Controlled Morphogenesis of Organic Polyhedral Nanocrystals from Cubes, Cubooctahedrons, to Octahedrons by Manipulating the Growth Kinetics

Longtian Kang,[†,‡] Hongbing Fu,*,[†] Xinqiang Cao,[†,‡] Qiang Shi,[†] and Jiannian Yao*,[†]

[†]Beijing National Laboratory for Molecular Sciences (BNLMS), Institute of Chemistry, Chinese Academy of Sciences, Beijing 100190, People's Republic of China

[‡]Graduate University of Chinese Academy of Sciences, Beijing 100039, People's Republic of China

Ⓢ Supporting Information

ABSTRACT: Morphological control of organic nanocrystals (ONCs) is important in the fields ranging from specialty chemicals to molecular semiconductors. Although the thermodynamic shape can be readily predicted, most growth morphologies of ONCs are actually determined by kinetic factors and remain poorly understood. On the basis of the reduction of zinc tetraphenylporphyrin perchlorate ($ZnTPP^+ClO_4^-$) with sodium nitrite ($Na^+NO_2^-$), we synthesized two series of ONCs of aquozinc tetraphenylporphyrin ($ZnTPP \cdot H_2O$), in the presence of either cetyltrimethylammonium bromide (CTAB) or poly(vinyl pyrrolidone) (PVP) as the capping ligands. As the cationic precursors of $ZnTPP^+$ are separated in the solution phase, smoothly

controlled release of $ZnTPP \cdot H_2O$ building blocks via the reduction reaction facilitates the separation between the nucleation and growth stages during the formation of ONCs and provides a high and tunable supersaturation unavailable by employing conventional crystallization techniques. We found that CTAB mainly serve as the colloidal stabilizer, while selective adhesion of PVP on the {020}s facet alters the crystal habits significantly. In both cases, manipulation of the growth kinetics had been achieved by adjusting the concentration of $ZnTPP \cdot H_2O$ growth units, and consequently, the supersaturation for the crystallization, thus yielding ONCs with well-controlled sizes and shapes. Remarkably, thermodynamically stable octahedrons have been obtained at high supersaturation in both CTAB and PVP cases.
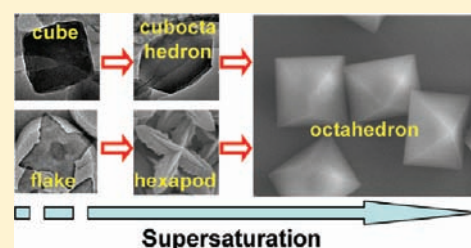
■ INTRODUCTION

Controlled synthesis of inorganic semiconductor and/or metal nanocrystals with well-defined sizes, shapes, and compositions had provided a powerful tool for tailoring their properties[1] and paved the way for far-reaching applications ranging from optoelectronics,[2] catalysis,[3] plasmonics,[4] to medical diagnostics.[5] Organic molecular crystals are fundamentally different from inorganic ones, because of weak van der Waals intermolecular interactions.[6] The growth morphology of organic nanocrystals (ONCs) coupled with its size are of great importance for industrial separation, purification, and storage processes;[7] moreover, they play a crucial role in developing novel organic semiconductor technologies,[8] such as single-crystal nanolasers,[9] transistor arrays,[10] sensors, and photoconductors.[11] However, although tailor-made molecules can generally be obtained by organic synthesis, the controlled synthesis of ONCs lags far behind their inorganic counterparts.[1,12]

The synthesis of organic molecules relies on the strength of covalent bond connecting between atoms, whereas organic molecular crystals are held together by a multitude of weak intermolecular interactions, thus often referred to as "supermolecule(s) par excellence".[13] The internal structure and symmetry of organic crystals might be engineered by focusing on the molecular recognition events between constituent molecular building blocks.[13,14] Ensuring that molecular components aggregate in a specific way and thus generate ONCs with a desirable size, shape, and therefore function,

however, remains a great challenge.[15] This is because most shapes of ONCs are actually controlled by the kinetics of the molecular growth process through which assembly occurs.[16] Arresting kinetically stable topology by controlling the nucleation and subsequent growth kinetics has been applied as a successful strategy for generating inorganic nanocrystals of various shapes.[12b] In particular, dot-, rod-, spindle-, and tetrapod-shaped semiconductor quantum dots have been synthesized by adjusting the monomer concentration using the sol method.[17] And cube, cubooctahedra, and octahedra of nobel metals have been fabricated by changing the precursor ratio and introducing surfactants as the shape controller in the polyol process.[18] Nonetheless, the effects of kinetic control on the growth morphologies of ONCs remain largely unexplored, partially due to the limited tuning range available for conventional solution crystallization process.

Herein, by employing the colloid chemical reaction method,[19] two series of ONCs of aquozinc tetraphenylporphyrin ($ZnTPP \cdot H_2O$) with well-controlled sizes and shapes had been synthesized on the basis of the reduction of zinc tetraphenylporphyrin perchlorate ($ZnTPP^+ClO_4^-$) with sodium nitrite ($Na^+NO_2^-$), in the presence of either cetyltrimethylammonium bromide (CTAB) and poly(vinyl pyrrolidone) (PVP) as the capping ligand. As the cationic

precursors are separated from each other in the solution phase, smoothly controlled release of neutral molecular building blocks via the reduction reaction facilitates the separation between the nucleation and growth stages during the formation of ONCs and provides a high and tunable supersaturation unavailable by employing conventional crystallization techniques. We found that the capping ligands of CTAB mainly serve as a colloidal stabilizer, while selective adhesion of PVP on the $\{020\}$s facet alters the crystal habits significantly. In both cases, manipulation of the growth kinetics had been achieved by adjusting the concentration of $ZnTPP \cdot H_2O$ growth units, yielding ONCs with well-controlled sizes and shapes. Remarkably, thermodynamically favorable octahedrons have been obtained at high supersaturation in both CTAB and PVP cases.

■ RESULTS

In a typical synthesis, precursors of $ZnTPP^+ClO_4^-$ were first synthesized via reaction 1:[20]

$$2ZnTPP + 2Ag^+ClO_4^- + I_2 \longrightarrow$$
$$2ZnTPP^+ClO_4^- + 2AgI \text{ (s)} \qquad (1)$$
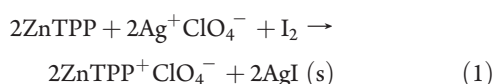
Next, 1 mL of 1 mM $ZnTPP^+ClO_4^-$ solution in anhydrous acetonitrile was rapidly injected into different volumes (V_{NaNO2}) of 10 mM $Na^+NO_2^-$ aqueous solution containing predissolved CTAB or PVP as the capping ligands. Following the reduction of $ZnTPP^+$ by NO_2^- via reaction 2:

$$2ZnTPP^+ClO_4^- + Na^+NO_2^- + 3H_2O \longrightarrow$$
$$2ZnTPP \cdot H_2O \text{ (s)} + Na^+NO_3^- + 2H^+ClO_4^- \qquad (2)$$
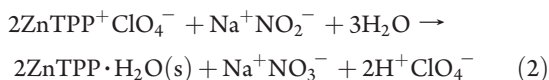
newly generated neutral $ZnTPP \cdot H_2O$ molecules undergo nucleation and growth, giving rise to ONCs. In our experiments, the reductant of $Na^+NO_2^-$ was stoichiometrically excessive, while the amount of $ZnTPP^+ClO_4^-$ was fixed at 1.0 mL of 1.0 mM. Therefore, the amount of $ZnTPP \cdot H_2O$ molecules produced via reaction 2 is actually the same in all samples. Consequently, the monomer concentration of $ZnTPP \cdot H_2O$ molecules (C_{ZnTPP}) can be easily adjusted as a function of V_{NaNO2}, according to $C_{ZnTPP} = 1.0 \div (1.0 + V_{NaNO2})$ mM. We found that the sizes and shapes of $ZnTPP \cdot H_2O$ ONCs were sensitive to the value of C_{ZnTPP} as well as the capping ligands of either CTAB or PVP presented in the system.

CTAB as the Capping Ligand. Figures 1−4 depict the morphology evolution pathway of $ZnTPP \cdot H_2O$ ONCs as a function of C_{ZnTPP}, in the presence of CTAB (5 mM) surfactant. If $C_{ZnTPP} < 0.120$ mM, no particles are detectable. At $C_{ZnTPP} = 0.120-0.125$ mM, it reaches the nucleation threshold, generating amorphous nanoparticles of 51 ± 4 nm in diameter (Figure S2). In the range of $C_{ZnTPP} = 0.143-0.167$ mM, transition from amorphous to crystalline structures leads to the formation of nanocubes with a side-length controllable from 100 ± 5 nm at $C_{ZnTPP} = 0.143$ mM (Figure 1A) to 203 ± 9 nm at $C_{ZnTPP} = 0.167$ mM (Figure 1B and C). Because of the uniformity of their size and shape, these nanocubes are able to self-assemble into ordered three-dimensional arrays on the supporting substrate (Figures 1A−C). Figure 1E displays the selected area electron diffraction (SAED) pattern recorded by directing the electron beam perpendicular to the flat square surface of a single cube (Figure 1D). Monoclinic $ZnTPP \cdot H_2O$ crystal (CCDC no.: ZNTPOR03) belongs to the space group of $C2$, with cell parameters of $a = 18.903(4)$ Å, $b = 9.672(2)$ Å, $c = 13.379(3)$ Å, $\alpha = \gamma = 90°$, $\beta = 134.922(3)°$. The nearly square symmetry of SAED
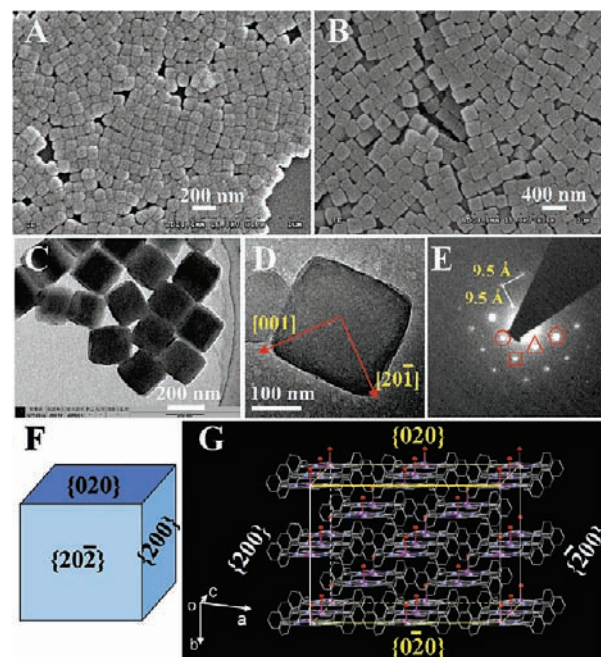

Figure 1. Scanning electron microscopy (SEM) images of nanocubes with an edge length of (A) 100 ± 5 nm prepared at $C_{ZnTPP} = 0.143$ mM and (B) 203 ± 9 nm prepared at $C_{ZnTPP} = 0.167$ mM, in the presence of CTAB surfactant. (C) Transmission electron microscopy (TEM) image of 203 nm nanocubes. (E) SAED pattern taken from a single cube shown in (D). In (E), the circled and triangle sets of spots with similar d spacing values of 9.5 Å are due to $\{001\}$s and $\{20\bar{1}\}$s Bragg reflections, while squared and pentagon sets of spots with similar d spacing values of 6.7 Å are due to $\{200\}$s and $\{20\bar{2}\}$s Bragg reflections. (F) Schematic model for the cube. (G) Molecular packing arrangement of $ZnTPP \cdot H_2O$ in a cube, viewed almost perpendicular to the $\{20\bar{2}\}$s crystal plane.

pattern shows the single crystal structure of the cube (Figure 1D). The circled and triangle sets of spots with similar d spacing values of 9.5 Å are due to $\{001\}$s (including $\{001\}$ and $\{00\bar{1}\}$) and $\{20\bar{1}\}$s (including $\{20\bar{1}\}$ and $\{\bar{2}01\}$) Bragg reflections ($d_{\{001\}s} = 9.47$ Å, $d_{\{20\bar{1}\}s} = 9.45$ Å, and $\angle\{001\}/\{20\bar{1}\} = 90°$); thereby, squared and pentagon sets of spots with similar lattice spacing values of 6.7 Å are assigned to reflections from $\{200\}$s (including $\{200\}$ and $\{\bar{2}00\}$) and $\{20\bar{2}\}$s (including $\{20\bar{2}\}$ and $\{\bar{2}02\}$) crystal planes ($d_{\{200\}s} = d_{\{20\bar{2}\}s} = 6.7$ Å and $\angle\{200\}/\{20\bar{2}\} = 90°$). Correlation of Bragg reflections identified in Figure 1E with the orientation of the cube shown in Figure 1D makes it clear that the cube is bound by $\{200\}$s and $\{20\bar{2}\}$s facets on the side surfaces and by $\{020\}$s (including $\{020\}$ and $\{0\bar{2}0\}$) facets on the top and bottom surfaces (Figure 1F). Figure 1G presents the packing arrangement of $ZnTPP \cdot H_2O$ molecules in the cube, viewed almost perpendicular to the $\{20\bar{2}\}$s crystal plane. As one can see, $ZnTPP \cdot H_2O$ molecules arrange themselves with the molecular plane parallel to $\{020\}$s crystal facet and perpendicular to $\{200\}$s and $\{20\bar{2}\}$s facets. [Note that the molecular arrangements of $ZnTPP \cdot H_2O$ within $\{200\}$s and $\{20\bar{2}\}$s crystal planes are almost the same (Figure S3).] The fact that SAED patterns measured for different single cubes are quite similar indicates that the $\{020\}$s faces of nanocubes are parallel to the supporting substrate. As evidenced by X-ray diffraction (XRD) measurement (Figure 2), this preferential orientation of nanocubes on the substrate enhances the relative intensity of $\{020\}$s diffraction peak. The ratio between the intensities of the $\{020\}$s and $\{100\}$s (or $\{11\bar{1}\}$s) diffraction peaks is 2.8 in the nanocube spectrum
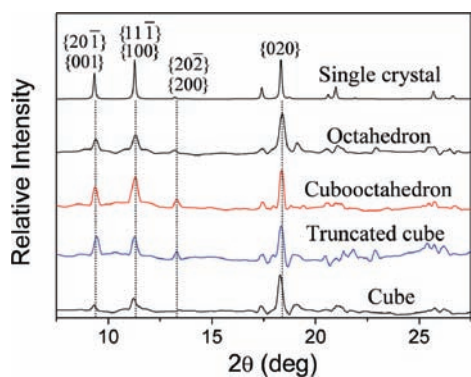
Figure 2. XRD patterns of cubes, truncated cubes, cubooctahedrons, and octahedrons, prepared in the presence of CTAB surfactant. The top line shows the standard powder spectrum simulated on the basis of the single crystal data by using the DIAMOND software.
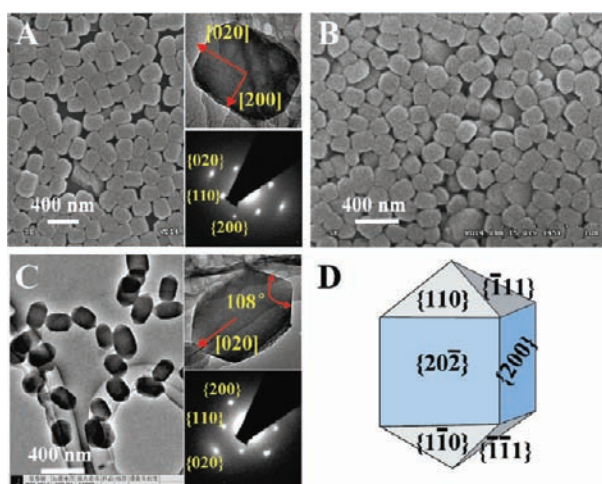
Figure 3. SEM images of (A) truncated cubes (width, 195 ± 12 nm and length, 195 ± 12 nm) prepared at C_{ZnTPP} = 0.182 mM, and (B) cubooctahedrons (width, 135 ± 7 nm and length, 218 ± 18 nm) prepared at C_{ZnTPP} = 0.200 mM. (C) TEM image of cubooctahedrons. The right bottom insets in (A) and (C) are SAED patterns taken from the single ONCs shown in the right top insets. (D) Schematic model for the cuboctahedron.

(the bottom line in Figure 2), much higher than the standard value of 1.0 (the top line in Figure 2).

The evolution of nanocubes into truncated ones with a width 195 ± 12 nm and a length of 246 ± 15 nm is observed at C_{ZnTPP} ≥ 0.182 mM (Figure 3A). According to the SAED pattern (the bottom inset of Figure 3A), the short and long axes of truncated tube are along the [020]s and [200]s (or [20$\bar{2}$]s) directions (the top inset of Figure 3A), respectively. The rapid growth along the [020]s direction finally eliminates itself, resulting in single crystal cubooctahedron at C_{ZnTPP} = 0.200 mM, which has a width of 135 ± 7 nm and a length of 218 ± 18 nm (Figure 3B and C). The SAED patterns of truncated cube and cubooctahedron, shown in the bottom insets of Figure 3A and C, respectively, confirm that the eight truncated crystal facets are {110}s and {11$\bar{1}$}s series of facets (Figure 3D). To keep the balance and lower the position of center-of-gravity, both truncated cubes and cubooctahedrons sit on the supporting substrate with their {200}s or {20$\bar{2}$}s faces. Indeed, it can be seen from Figure 2 that the relative intensity of the {200}s (or {20$\bar{2}$}s)
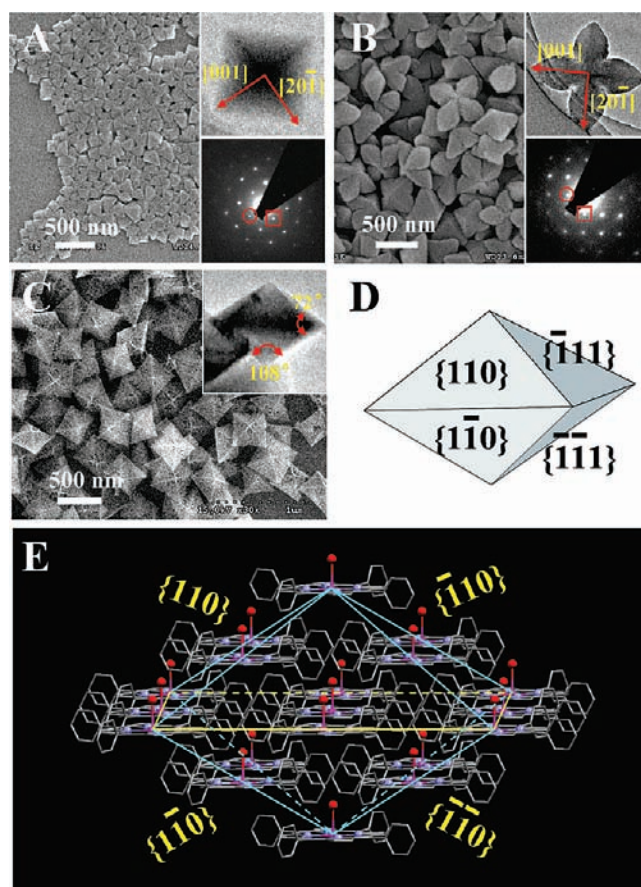
Figure 4. SEM images of octahedrons with controllable sizes prepared at C_{ZnTPP} = (A) 0.250, (B) 0.500, and (C) 0.667 mM, respectively. The right bottom insets in (A) and (B) are SAED patterns taken from single octahedrons shown in the right top insets. The circled and squared sets of spots are due to {001}s and {20$\bar{1}$}s Bragg reflections. The inset in (C) shows the TEM image of a single octahedron. (D) Schematic model for octahedron. (E) Molecular packing arrangement of ZnTPP·H₂O in an octahedron.

diffraction peak is enhanced in the spectra of truncated cubes and cubooctahedrons. By increasing C_{ZnTPP} further to 0.25 mM, single crystal octahedrons with an edge-length of 246 ± 15 nm are formed (Figure 4A). Further growth from the six corners of an octahedron takes place as shown in Figure 4B at C_{ZnTPP} = 0.500 mM (Figure 4B), finally leading to larger octahedrons with an edge-length of 417 ± 15 nm at C_{ZnTPP} = 0.667 mM (Figure 4C). Combining with the results of cubooctahedrons, Figure 4D shows a schematic representation for an octahedron. Note that the dihedral angles measured for a octahedron in the inset of Figure 4C are consistent with the crystallographic data, that is, ∠{110}/{1$\bar{1}$0} (or ∠{11$\bar{1}$}/{1$\bar{1}\bar{1}$})=71.8°, and ∠{110}/{$\bar{1}$10} (or ∠{11$\bar{1}$}/{$\bar{1}$11})=108.2° (Figure 4E).

PVP as the Capping Ligand. As shown in Figure 5, we observed a different morphology evolution pathway of ZnTPP·H₂O crystals if PVP (fixed at 0.1 M in repeating units in all the reaction mixtures) is selected as the capping ligand. Primary nanoparticles with a diameter of 36 ± 4 nm are not formed until C_{ZnTPP} reaches 0.140−145 mM (Figure 5A), indicating a higher nucleation threshold in PVP than that in CTAB (0.120−125 mM). At C_{ZnTPP} = 0.167 mM, square nanoflakes are formed with a side-length of 342 ± 15 nm and a thickness of 51 ± 5 nm (Figure 5B). Also confirmed by TEM image (inset of Figure 5B), these square nanoflakes are able to
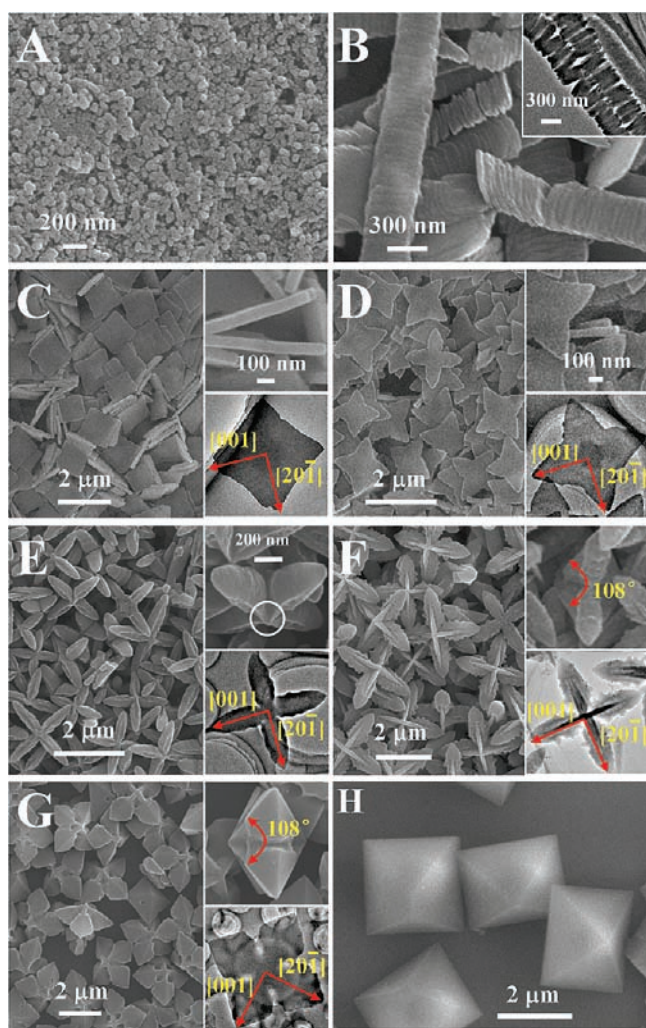
Figure 5. SEM images of ZnTPP·H$_2$O ONCs prepared at C_{ZnTPP} = (A) 0.143 (particles), (B) 0.167 (square flakes), (C) 0.200 (square flakes), (D) 0.222 (planar tetrapods), (E) 0.250 (crosses), (F) 0.333 (hexapods), (G) 0.500 (growing octahedrons), and (H) 0.667 mM (octahedrons), respectively, in the presence of PVP (fixed at 0.1 M in repeating units in all the reaction mixtures) as the capping ligand. The inset in (B) is the TEM image of 1D self-assembly of square nanoflakes. The right top and bottom insets in (C)−(G) are the corresponding high-magnification SEM and TEM images, respectively.

self-assemble into ordered 1D array rather than 3D self-assembly observed for cubes. The SAED pattern reveals that square nanoflake (Figure S4) is similar to nanocubes, also bounded by {020}s, {200}s, and {20$\bar{2}$}s series of facets. However, the aspect ratio of the former (6.7) is much higher than that of the latter (1.0), suggesting that the growth along the [020]s direction is seriously restricted in nanoflakes. The aspect ratio of square flakes adds up to 13 at C_{ZnTPP} = 0.200 mM (Figure 5C); meanwhile, these nanoflakes with a side-length of 1131 ± 74 nm and a thickness of 87 ± 7 nm lose the ability to 1D self-assemble (Figure 5C). These results demonstrate clearly that the self-assembling behavior of ZnTPP·H$_2$O ONCs strongly depends on its shape and size.

Under conditions of C_{ZnTPP} > 0.200 mM, preferential growth along the [001]s and [20$\bar{1}$]s directions makes the shape of ZnTPP·H$_2$O single crystals like a planar-tetrapod at C_{ZnTPP} = 0.222 mM (Figures 5D and S5) and even like a cross at C_{ZnTPP} = 0.250 mM (Figures 5E and S6). More than 30% of square flakes
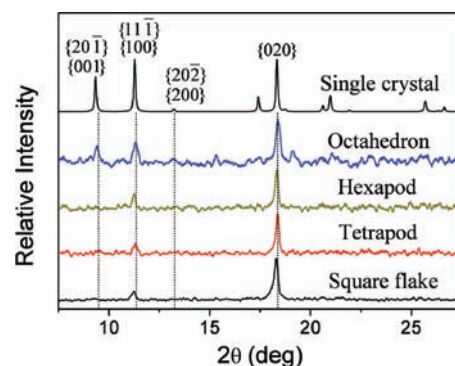
Figure 6. XRD patterns of square flakes, planar-tetrapods, hexapods, and octahedrons, prepared in the presence of PVP as the capping ligand. The top line shows the standard powder spectrum simulated on the basis of the single crystal data by using the DIAMOND software.

and planar-tetrapod present a semispherical core, as indicated by TEM images in the bottom insets of Figure 5C and D. This confirms that they are developed from particles. The side-length and thickness of planar-tetrapods (Figure 5C) are similar to those of square flakes (Figure 5D), whereas the crosses become larger with a diagonal-length of 1994 ± 89 nm and a thickness of 398 ± 35 nm (Figure 5E and S6). The serious restriction of the growth along the [020]s direction in flake, planar-tetrapod, and cross shrinks those surfaces bounded by {hkl} facets with k = 0, such as {200}s, {20$\bar{2}$}s, {001}s, and {20$\bar{1}$}s. Therefore, it can be seen from Figure 6 that the {200}s (or {20$\bar{2}$}s) and {001}s (or {20$\bar{1}$}s) XRD peaks, which are clearly resolved in the spectrum of cubes (Figure 2), are actually absent from the spectra of flake, planar-tetrapod, and cross, indicating these faces are less abundant on the surfaces.

The top {020}s faces of flakes and planar-tetrapods appear quite smooth, but grooves are present along diagonals of the cross (Figures 5E and S6). By increasing C_{ZnTPP} to 0.333 mM (Figure 5F), pairs of triangular sheets rise up in a steep wall from rough diagonal grooves of top and bottom sides of the cross, probably directed by the growth along [020]s directions as shown by the white circle in the top inset of Figure 5E. The overall shape resembles a hexapod that factually provides a backbone for an octahedron (top inset of Figure 5F and Figure S7). Indeed, single crystal octahedrons are formed at C_{ZnTPP} = 0.667 mM (Figure 5H) based on the hexapod via a fill-in mechanism, as suggested by the quasi-octahedron obtained at C_{ZnTPP} = 0.500 mM (Figures 5G and S8). Factually, the sizes of hexapods, quasi−octahedrons, and octahedrons are similar with an edge-length of 2420 ± 180 nm.

■ DISCUSSION

In our experiments, we changed the total volume of the reaction mixture to adjust the monomer concentration of C_{ZnTPP}, and, consequently, the supersaturation (σ), according to $\sigma = C_{ZnTPP}/C_{eq}$, where C_{ZnTPP} and C_{eq} represent the actual concentration and the equilibrium concentration of ZnTPP·H$_2$O molecules in the coexistence phase.[21] By assuming C_{eq}(CTAB) = 0.120 mM and C_{eq}(PVP) = 0.140 mM, Table 1 summarizes the morphology variations of ZnTPP·H$_2$O ONCs as a function of the value of σ in both CTAB and PVP cases.

Predicted Equilibrium and Growth Morphologies. To gain further insight into the mechanistic basis, the equilibrium shape of ZnTPP·H$_2$O crystal for minimum total surface energy has been calculated by using the software of the Material Studio

1898

dx.doi.org/10.1021/ja108730u |*J. Am. Chem. Soc.* 2011, 133, 1895–1901

Table 1. Summary of Shapes of ZnTPP·H₂O ONCs as a Function of the Value of σ, Prepared in the Presence of Either CTAB or PVP in the System

V_{NaNO2} (mL)	C_{ZnTPP} (mM)	CTAB as the capping ligand			PVP as the caping ligand		
		σ^a	region[b]	shape	σ^a	region[b]	shape
7.0	0.125	1.04	I	particle			
6.0	0.143	1.19	II	cube	1.02	I	particle
5.0	0.167	1.39	II	cube	1.19	II	square plates
4.5	0.182	1.52	III	truncated cube			
4.0	0.200	1.67	III	cuboctahedron	1.43	II	square plates
3.5	0.222				1.59	III	planar-tetrapod
3.0	0.250	2.08	III	octahedron	1.78	III	cross
2.0	0.333	2.78	III	quasi-octahedron	2.38	IV	hexapod
1.0	0.500				3.57	IV	quasi-octahedron
0.5	0.667	5.56	III	octahedron	4.76	IV	octahedron

^{a} The supersaturation σ is calculated according to $\sigma = C_{ZnTPP}/C_{eq}$, and $C_{eq} = 0.120, 0.40$ mM for CTAB, PVP, respectively. ^{b} The roman numerals label the region of the supersaturation σ, in which ONCs with a specific shape are generated.

Table 2. Surface Free ($\gamma_{\{hkl\}}$) and Attachment ($E_{\{hkl\}}^{attach}$) Energies of Various Crystal Facets $\{hkl\}$ Calculated by Using the Material Studio Package

$\{hkl\}$	$d_{\{hkl\}}$ (Å)	$\gamma_{\{hkl\}}$ (kcal/mol)	$E_{\{hkl\}}^{attach}$ (kcal/mol)
$\{11\bar{1}\}$s	7.84	33.5	−72.1
$\{110\}$s	7.84	33.8	−72.8
$\{20\bar{1}\}$s	9.45	45.4	−86.8
$\{001\}$s	9.47	48.7	−93.1
$\{020\}$s	4.84	50.5	−95.5
$\{200\}$s	6.69	75.5	−126.9
$\{20\bar{2}\}$s	6.69	75.5	−127.0

package.[21,22] The calculated surface energies ($\gamma_{\{hkl\}}$) of the various crystal faces $\{hkl\}$ follow the order: $\gamma_{\{200\}s} \approx \gamma_{\{20\bar{2}\}s} > \gamma_{\{020\}s} > \gamma_{\{001\}s} \approx \gamma_{\{20\bar{1}\}s} > \gamma_{\{110\}s} \approx \gamma_{\{11\bar{1}\}s}$ (Table 2), yielding an octahedron bound by low-energy $\{100\}$s and $\{11\bar{1}\}$s faces and truncated on all the six corners (Figure 7A). This suggests that octahedron-shaped morphology obtained at high supersaturation in both CTAB and PVP cases is the thermodynamically favorable one. The growth morphology, however, depends on the relative growth rates $R_{\{hkl\}}^{rel}$ of the crystal faces $\{hkl\}$.[16a,21] The widely adopted attachment energy model relates the energy ($E_{\{hkl\}}^{attach}$) released when two layers of the crystal structure $\{hkl\}$ are brought together to $R_{\{hkl\}}^{rel}$, according to $R_{\{hkl\}}^{rel} = A \times E_{\{hkl\}}^{attach}$, where A is a proportional constant.[23] Figure 7B illustrates that the predicted growth morphology based on the attachment energies (Table 2) is also an analogy of octahedron. As compared to the equilibrium shape (Figure 7A), $\{020\}$s faces are eliminated in the growth morphology besides the truncation on $\{001\}$s and $\{20\bar{1}\}$s facets (Figure 7B). Among the interplanar spacings $d_{\{hkl\}}$ in Table 2, $d_{\{020\}s} = 4.84$ Å is the shortest. Therefore, elimination of $\{020\}$s faces in the growth morphology suggests a preferential growth along the $[020]$s directions. In any event, the predicted growth morphology shown in Figure 7B is different from those shapes of ZnTPP·H₂O ONCs obtained at low supersaturation in both CTAB (Figures 1−3) and PVP (Figure 5) cases, which are actually bound by high-energy faces, such as $\{200\}$s, $\{20\bar{2}\}$s, and $\{020\}$s faces.

As above-mentioned, we controlled the growth shapes of ZnTPP·H₂O ONCs by adjusting the monomer concentration of C_{ZnTPP}, therefore, the supersaturation σ (Table 1), which represents the driving force for the crystallization ($\Delta\mu/k_B T$),
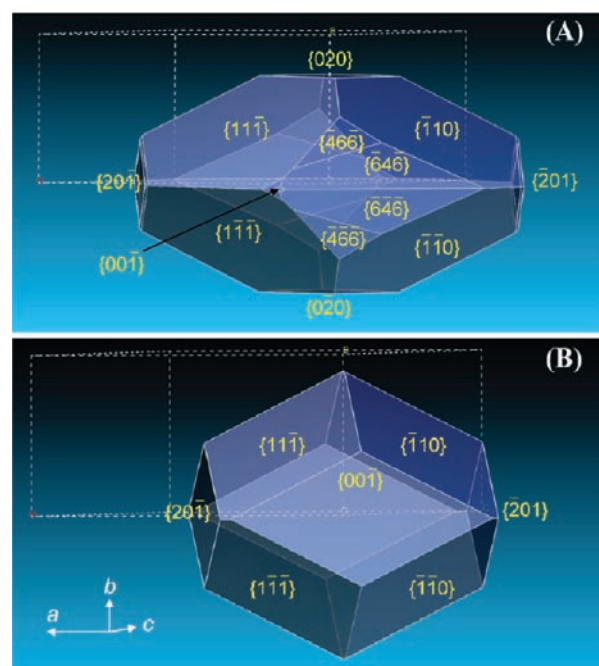
Figure 7. (A) The equilibrium shape of ZnTPP·H₂O crystal for minimum total surface energy and (B) the predicted growth morphology based on the attachment energies, calculated by using the software of Material Studio package.

according to $\Delta\mu = k_B T \ln(\sigma)$, where $\Delta\mu$ is the difference in chemical potential between the growth units of ZnTPP·H₂O in the crystal and the liquid phase, k_B is Boltzmann's constant, and T is the absolute temperature (298 K).[21] It must be noted that the treatment of $R_{\{hkl\}}^{rel}$ based on the attachment energy model, according to $R_{\{hkl\}}^{rel} = A \times E_{\{hkl\}}^{attach}$ (A is a proportional constant), does not include the driving force of $\Delta\mu/k_B T$.[23] This might be responsible for the inconsistency of the predicted growth morphology (Figure 7B) with the observed shapes of ZnTPP·H₂O ONCs at low supersaturation in both CTAB and PVP cases.

Kinetic Control on the Growth of ZnTPP·H₂O ONCs. As the crystallization is intrinsically a nonequilibrium process, the crystal shape can be dominated by the kinetics of the growth process.[14,16] The most important mechanisms, in which the

1899

dx.doi.org/10.1021/ja108730u |*J. Am. Chem. Soc.* 2011, 133, 1895–1901

supersaturation has been taken into account, are two-dimensional (2D) nucleation and spiral growth models.[16a,23b,24] For these two models, the relative growth rate $R^{rel}_{\{hkl\}}$ of the crystal face $\{hkl\}$ follows:

$$R^{rel}_{\{hkl\}} \propto C \times \exp(-\Delta G^{\ddagger}_{\{hkl\}}/k_B T) \qquad (3)$$

where C is the concentration of the growth units (C_{ZnTPP} in our system), and $\Delta G^{\ddagger}_{\{hkl\}}$ represents the activation free energy for the growth of the crystal face $\{hkl\}$.[16a,24] It can be seen that the ratio between the relative growth rates of $R^{rel}_{\{hkl\}}$ depends on the kinetic barriers $\Delta G^{\ddagger}_{\{hkl\}}$ for the growth of the crystals faces $\{hkl\}$. Generally, the higher is the surface energy of $\gamma_{\{hkl\}}$, the lower is the kinetic barrier of $\Delta G^{\ddagger}_{\{hkl\}}$. Therefore, the high-energy faces grow faster than the low-energy faces in most cases.[16a,23b,25] According to the calculated order of $\gamma_{\{hkl\}}$ (Table 2), the value of $\Delta G^{\ddagger}_{\{hkl\}}$ might follow the order: $\Delta G^{\ddagger}_{\{200\}s} \approx \Delta G^{\ddagger}_{\{20\bar{2}\}s} \approx \Delta G^{\ddagger}_{\{020\}s} \approx \Delta G^{\ddagger}_{\{001\}s} \approx \Delta G^{\ddagger}_{\{20\bar{1}\}s} \approx \Delta G^{\ddagger}_{\{110\}s} \approx \Delta G^{\ddagger}_{\{11\bar{1}\}s}$.

In our wet chemical method, the cationic precursors of $ZnTPP^+$ are separated in the solution phase. The growth units of neutral $ZnTPP \cdot H_2O$ molecules are gradually released via the reduction reaction 2. Once $\sigma \geq 1.0$ ($\Delta\mu/k_B T \geq 0$) reaches the nucleation threshold, a nucleation burst generates primary particles.[26] More and more growth units are then fed by the reduction of the remaining precursors. As long as the consumption of feedstock by the growing ONCs is not exceeded by the release rate of neutral growth units via the reduction reaction, no new nuclei form. Therefore, our colloidal chemical method facilitates the separation between the nucleation and growth stages during the formation of $ZnTPP \cdot H_2O$ ONCs.[19] Moreover, convenient adjustment of the precursor concentration provides a tunable supersaturation for manipulating the nucleation and growth kinetics. We indentified a critical value of $\sigma \approx 1.20$ in both CTAB and PVP cases (Table 1). If $\sigma < 1.20$ (region I for both CTAB and PVP parts in Table 1), particles are always obtained, but amorphous in nature probably because the chemical potential of the system ($\Delta\mu$) is too low to overcome any of $\Delta G^{\ddagger}_{\{hkl\}}$. If $\sigma \geq 1.20$ (region II for both CTAB and PVP parts in Table 1), the growth of $\{200\}s$ and $\{20\bar{2}\}s$ faces takes place as a result of $\Delta\mu \geq \Delta G^{\ddagger}_{\{200\}s} \approx \Delta G^{\ddagger}_{\{20\bar{2}\}s}$.

In the case of CTAB (see the CTAB part in Table 1),[27] cube-shaped ONCs are formed in the region II of $1.40-1.50 \geq \sigma \geq 1.20$. However, in the region III of $\sigma > 1.40-1.50$ (Table 1), the chemical potential of the system ($\Delta\mu$) is high enough to overcome the barrier of $\Delta G^{\ddagger}_{\{020\}s}$, making $R^{rel}_{\{020\}s} > R^{rel}_{\{200\}s} \approx R^{rel}_{\{20\bar{2}\}s}$. Accordingly, the rapid growth of $\{020\}s$ faces results in truncated cubes and cubooctahedrons. Once $\{020\}s$ faces grow out of existence, remained growth of $\{200\}s$ and $\{20\bar{2}\}s$ faces at high supersaturation finally eliminates itself, leaving octahedrons bounded by low-energy $\{100\}s$ and $\{11\bar{1}\}s$ facets (see the CTAB part in Table 1).

The situation is quite different in the case of PVP, because PVP molecules can interact strongly with ZnTPP molecules through hydrogen bonding.[28] It is the solubilization effect induced by PVP that results in a higher nucleation threshold concentration in the case of PVP ($C_{eq} = 0.140$ mM) than that in the case of CTAB ($C_{eq} = 0.120$ mM) (Table 1). Furthermore, PVP molecules might selectively adhere to $\{020\}s$ faces through hydrogen bonding between pyrrolidone groups of PVP and apical H_2O moieties of $ZnTPP \cdot H_2O$ exposed on $\{020\}s$ faces. The selective adhesion of PVP to $\{020\}s$ faces can lower the $\gamma_{\{020\}s}$, thus raising $\Delta G^{\ddagger}_{\{020\}s}$, leading to a decrease of $R^{rel}_{\{020\}s}$.[29] Indeed, square

nanoflakes, rather than nanocubes in the case of CTAB, are formed in the region II of $1.40-1.50 \geq \sigma \geq 1.20$ in the case of PVP (Table 1), due to the restriction of the growth of $\{020\}s$ faces. This selective adhesion of PVP to $\{020\}s$ faces even lowers $\gamma_{\{020\}s} < \gamma_{\{001\}s} \approx \gamma_{\{20\bar{1}\}s}$, thus raising $\Delta G^{\ddagger}_{\{020\}s} > \Delta G^{\ddagger}_{\{001\}s} \approx \Delta G^{\ddagger}_{\{20\bar{1}\}s}$. Therefore, under conditions of region III of $\sigma > 1.40-1.50$ (see the PVP part in Table 1), $\Delta G^{\ddagger}_{\{020\}s} > \Delta\mu > \Delta G^{\ddagger}_{\{001\}s} \approx \Delta G^{\ddagger}_{\{20\bar{1}\}s}$ results in the rapid growth along the $[001]s$ and $[20\bar{1}]s$ directions. It is $R^{rel}_{\{001\}s} \approx R^{rel}_{\{20\bar{1}\}s} > R^{rel}_{\{200\}s} \approx R^{rel}_{\{20\bar{2}\}s}$ that shapes $ZnTPP \cdot H_2O$ ONCs like a planar–tetrapod or a cross. In the region IV of $\sigma > 2.0-2.30$ (see the PVP part in Table 1), the growth barrier of $\{020\}s$ is eventually overcome. The explosive growth along the $[020]s$ directions generates a hexapod, which provides a backbone for filling-in $ZnTPP \cdot H_2O$ units to form the thermodynamically favorable octahedron.

CONCLUSIONS

By employing the colloid chemical reaction method, two series of ONCs of $ZnTPP \cdot H_2O$ with well-controlled sizes and shapes had been synthesized on the basis of the reduction of $ZnTPP^+ClO_4^-$ with $Na^+NO_2^-$, in the presence of either CTAB or PVP as the capping ligand. As the cationic precursors of $ZnTPP^+$ are separated from each other in the solution phase, smoothly controlled release of $ZnTPP \cdot H_2O$ building blocks via the reduction reaction facilitates the separation between the nucleation and growth stages of ONCs and provides a high and tunable supersaturation unavailable in conventional crystallization techniques. We found the capping ligand of CTAB mainly serves as a colloidal stabilizer, while selective adhesion of PVP on the $\{020\}$ facet significantly alters the crystal habits. In both cases, manipulation of the growth kinetics had been achieved by adjusting the concentration of $ZnTPP \cdot H_2O$ growth units, and, consequently, the supersaturation for the crystallization, thus yielding ONCs with well-controlled sizes and shapes. Nonetheless, thermodynamically favored octahedrons have been obtained at high supersaturation in both CTAB and PVP cases.

ASSOCIATED CONTENT

S **Supporting Information.** Precursor preparation, experimental procedures, characterization techniques, Material Studio calculations, and additional data and results. This material is available free of charge via the Internet at http://pubs.acs.org.

AUTHOR INFORMATION

Corresponding Author
hongbing.fu@iccas.ac.cn; jnyao@iccas.ac.cn

ACKNOWLEDGMENT

REFERENCES

(1) Burda, C.; Chen, X. B.; Narayanan, R.; El-Sayed, M. A. *Chem. Rev.* **2005**, *105*, 1025.
(2) (a) Huynh, W. U.; Dittmer, J. J.; Alivisatos, A. P. *Science* **2002**, *295*, 245. (b) Sun, Q.; Wang, Y. A.; Li, L. S.; Wang, D. Y.; Zhu, T.; Xu, J.; Yang, C. H.; Li, Y. F. *Nat. Photon.* **2007**, *1*, 717.

(3) (a) Bell, A. T. *Science* **2003**, *299*, 1688. (b) Niu, Y. H.; Yeung, L. K.; Crooks, R. M. *J. Am. Chem. Soc.* **2001**, *123*, 6840.

(4) (a) Kelly, K. L.; Coronado, E.; Zhao, L. L.; Schatz, G. C. *J. Phys. Chem. B* **2003**, *107*, 668. (b) Jin, R. C.; Cao, Y. W.; Mirkin, C. A.; Kelly, K. L.; Schatz, G. C.; Zheng, J. G. *Science* **2001**, *294*, 1901.

(5) (a) Huang, X. H.; El-Sayed, I. H.; Qian, W.; El-Sayed, M. A. *J. Am. Chem. Soc.* **2006**, *128*, 2115. (b) Jiang, W.; Kim, B. Y. S.; Rutka, J. T.; Chan, W. C. W. *Nat. Nanotechnol.* **2008**, *3*, 145.

(6) (a) Silinsh, E. A. *Organic Molecular Crystals: Their Electronic States*; Springer-Verlag: Berlin, 1980. (b) Pope, M.; Swenberg, C. E. *Electronic Processes in Organic Crystals and Polymers*; Oxford University Press: Oxford, 1999.

(7) (a) Rodriguez-Hornedo, N.; Murphy, D. *J. Pharm. Sci.* **1999**, *88*, 651. (b) Docherty, R.; Clydesdale, G.; Roberts, K. J.; Bennema, P. *J. Phys. D: Appl. Phys.* **1991**, *24*, 89.

(8) (a) Sundar, V. C.; Zaumseil, J.; Podzorov, V.; Menard, E.; Willett, R. L.; Someya, T.; Gershenson, M. E.; Rogers, J. A. *Science* **2004**, *303*, 1644. (b) Liu, S. H.; Wang, W. C. M.; Briseno, A. L.; Mannsfeld, S. C. B.; Bao, Z. N. *Adv. Mater.* **2009**, *21*, 1217. (c) Nakanishi, H.; Oikawa, H. In *Single Organic Nanoparticles*; Masuhara, H., Nakanishi, H., Sasaki, K., Eds.; Springer-Verlag: New York, 2003; Chapter 2, pp 17−31. (d) Zang, L.; Che, Y. K.; Moore, J. S. *Acc. Chem. Res.* **2008**, *41*, 1596. (e) Zhao, Y. S.; Fu, H. B.; Peng, A. D.; Ma, Y.; Liao, Q.; Yao, J. N. *Acc. Chem. Res.* **2010**, *43*, 109. (f) Li, I. J.; Hu, W. P.; Liu, Y. Q.; Zhu, D. B. *Acc. Chem. Res.* **2010**, *43*, 529. (g) Zhang, X. J.; Dong, C.; Zapien, J. A.; Ismathullakhan, S.; Kang, Z. H.; Jie, J. S.; Zhang, X. H.; Chang, J. C.; Lee, C. S.; Lee, S. T. *Angew. Chem., Int. Ed.* **2009**, *48*, 9121.

(9) (a) Samuel, I. D. W.; Turnbull, G. A. *Chem. Rev.* **2007**, *107*, 1272. (b) Zhao, Y. S.; Peng, A. D.; Fu, H. B.; Ma, Y.; Yao, J. N. *Adv. Mater.* **2008**, *20*, 1661. (c) O'Carroll, D.; Lieberwirth, I.; Redmond, G. *Nat. Nanotechnol.* **2007**, *2*, 180.

(10) (a) Briseno, A. L.; Mannsfeld, S. C. B.; Lin, M. M.; Liu, S. H.; Tseng, R. J.; Reese, C.; Roberts, M. E.; Yang, Y.; Wudl, F.; Bao, Z. N. *Nature* **2006**, *444*, 913. (b) Nelson, S. F.; Lin, Y. Y.; Gundlach, D. J.; Jackson, T. N. *Appl. Phys. Lett.* **1998**, *72*, 1854. (c) Luo, L.; Liu, G.; Huang, L. W.; Cao, X. Q.; Liu, M.; Fu, H. B.; Yao, J. N. *Appl. Phys. Lett.* **2009**, *95*, 263312.

(11) (a) Che, Y. K.; Yang, X. M.; Lin, G. L.; Yu, C.; Ji, H. W.; Zuo, J. M.; Zhao, J. C.; Zang, L. *J. Am. Chem. Soc.* **2010**, *132*, 5743. (b) Zhao, Y. S.; Wu, J. S.; Huang, J. X. *J. Am. Chem. Soc.* **2009**, *131*, 3158.

(12) (a) Murray, C. B.; Kagan, C. R.; Bawendi, M. G. *Annu. Rev. Mater. Sci.* **2000**, *30*, 545. (b) Yin, Y. D.; Alivisatos, A. P. *Nature* **2005**, *437*, 664.

(13) (a) Moulton, B.; Zaworotko, M. J. *Chem. Rev.* **2001**, *101*, 1629. (b) Weissbuch, I.; Addadi, L.; Lahav, M.; Leiserowitz, L. *Science* **1991**, *253*, 637. (c) Zaworotko, M. J. *Cryst. Growth Des.* **2007**, *7*, 4.

(14) (a) Hollingsworth, M. D. *Science* **2002**, *295*, 2410. (b) Desiraju, G. R. *Nat. Mater.* **2002**, *1*, 77. (c) Braga, D.; Brammer, L.; Champness, N. R. *CrystEngComm* **2005**, *7*, 1.

(15) (a) Jonkheijm, P.; van der Schoot, P.; Schenning, A. P. H. J.; Meijer, E. W. *Science* **2006**, *313*, 80. (b) Wang, Y. B.; Fu, H. B.; Peng, A. D.; Zhao, Y. S.; Ma, J. S.; Ma, Y.; Yao, J. N. *Chem. Commun.* **2007**, 1623.

(16) (a) Liu, X. Y.; Boek, E. S.; Briels, W. J.; Bennema, P. *Nature* **1995**, *374*, 342. (b) Huang, L. W.; Liao, Q.; Shi, Q.; Fu, H. B.; Ma, J. S.; Yao, J. N. *J. Mater. Chem.* **2010**, *20*, 159. (c) Lei, Y. L.; Liao, Q.; Fu, H. B.; Yao, J. N. *J. Phys. Chem. C* **2009**, *113*, 10038.

(17) (a) Peng, Z. A.; Peng, X. G. *J. Am. Chem. Soc.* **2001**, *123*, 1389. (b) Peng, Z. A.; Peng, X. G. *J. Am. Chem. Soc.* **2002**, *124*, 3343. (c) Manna, L.; Scher, E. C.; Alivisatos, A. P. *J. Am. Chem. Soc.* **2000**, *122*, 12700.

(18) (a) Tao, A.; Sinsermsuksakul, P.; Yang, P. D. *Adv. Mater.* **2006**, *45*, 4597. (b) Tsung, C. K.; Kuhn, J. N.; Huang, W. Y.; Aliaga, C.; Huang, L. I.; Somorjai, G. A.; Yang, P. D. *J. Am. Chem. Soc.* **2009**, *131*, 5816.

(19) Kang, L. T.; Wang, Z. C.; Cao, Z. W.; Ma, Y.; Fu, H. B.; Yao, J. N. *J. Am. Chem. Soc.* **2007**, *129*, 7305.

(20) Shine, H. J.; Padilla, A. G.; Wu, S. M. *J. Org. Chem.* **1979**, *44*, 4069.

(21) Sunagawa, I. *Crystals: Growth, Morphology and Perfection*; Cambridge University Press: Cambridge, 2005.

(22) Mann, S. *Angew. Chem., Int. Ed.* **2000**, *39*, 3392.

(23) (a) Bennema, P.; van der Eerden, J. P. *Morphology of Crystals*; Terra Scientific (TERRPUB): Tokyo, 1987; pp 1−75. (b) Boerrigter, S. X. M.; Cuppen, H. M.; Ristic, R. I.; Sherwood, J. N.; Bennema, P.; Meekes, H. *Cryst. Growth Des.* **2002**, *2*, 357.

(24) Mullin, J. W. *Crystallization*, 3rd ed.; Butterworth Heinemann: Oxford, 1992; Chapter 6, pp 202−260.

(25) Lee, S. M.; Cho, S. N.; Cheon, J. W. *Adv. Funct. Mater.* **2003**, *15*, 441.

(26) Lamer, V. K.; Dinegar, R. H. *J. Am. Chem. Soc.* **1950**, *72*, 4847.

(27) It has been established that as-formed particles can be stabilized by the formation of a protective layer of CTAB through hydrophobic interactions (ref 19), which are non-selective with regard to different crystal faces. Moreover, CTAB surfactant molecules that adhere to ONCs' surface are dynamically exchangeable, allowing the growth units on (growth) and off (dissolution) the growing ONCs. See the reference: Lei, Y. L.; Liao, Q.; Fu, H. B.; Yao, J. N. *J. Am. Chem. Soc.* **2010**, *132*, 1742.

(28) Viseu, T. M. R.; Hungerford, G.; Coelho, A. F.; Ferreira, M. I. C. *J. Phys. Chem. B* **2003**, *107*, 13300.

(29) Sun, Y. G.; Xia, Y. N. *Science* **2002**, *298*, 2176.